A General Solution to Wireless Power Transfer between Two Circular Loops

Ada S. Y. Poon[*]

Abstract—Wireless power transmission has been analytically studied in near-field coupling systems based on the small-antenna and near-field approximations, and in microwave power beaming systems based on the far-field approximation. This paper attempts to provide a general solution based on full-wave analysis to wireless power transmission between two circular loops. The solution applies to arbitrary transmit and receive loop radii, transmission range, orientation and alignment of the loops, and dielectric properties in a homogeneous isotropic medium. The power link is modeled as a two-port network and the efficiency based on simultaneous conjugate matching is used as the performance metric. The self and mutual admittances are analytically solved by expressing the current on the loops in Fourier series and the fields in vector spherical wave functions, and by the use of vector addition theorem to relate the coupling between the loops. The general solution is then applied to draw new insights such as the optimal carrier frequency between symmetric loops and impact of higher order modes on the power transfer efficiency between asymmetric loops.

1. INTRODUCTION

The concept of wireless power transfer has been introduced since the 19th century. In 1890's, Tesla demonstrated the first near-field coupling system that wirelessly powered a lamp based on a two-coil system [1, 2]. Resonant circuits were used to enhance the transmission range. More than a hundred years later, researchers from MIT introduced a four-coil system and performed similar experiment [3, 4]. The additional two coils, one at the transmitter and one at the receiver, function as impedance transformers to match the generator impedance with the self impedance of the primary coil, and to match the load impedance of the lamp with the self impedance of the secondary coil, respectively. The near-field coupling system as the name suggested, operates in the near field. To increase the transmission range, far-field methods were investigated. Brown et al. demonstrated beamed microwave power transmission to wirelessly power a helicopter in flight of 60 ft above the transmit aperture and thereafter, assessed the concept of solar power satellite (SPS) [5, 6].

In near-field coupling, the dimension of the coils and the transmission range are comparable, and they are much less than a wavelength. The coupling is dominated by the TE_{10} mode of the coils and the transmission can be analytically solved by the near-field approximation. In microwave power beaming, on the other hand, the transmission range is much larger than the dimension of the apertures. The dimension can be on the order of or much greater than a wavelength. The coupling is dominated by the resonant mode of the apertures and the transmission are analytically solved by the far-field approximation. When neither of those conditions is satisfied, for example, the dimension of the coils or the transmission range is on the order of a wavelength, there is no analytical solution reported in the literature. This paper attempts to provide a general solution that applies to arbitrary dimension of the coils, transmission range, alignment between the coils, and dielectric properties in a homogeneous isotropic medium.

Our analytical framework is based on a general two-port representation of the coupling between two circular loops. As circular loop is one of the fundamental antenna structures, the self and mutual admittances of two circular loops have been studied extensively. In [7], it evaluated the self and mutual admittances of two coaxial, identical circular loops. The result was extended to an array of coaxial circular loops with arbitrary radii [8]. In [9], an array of loops of arbitrary radii and orientation were considered. The coupling between loops was derived through coordinate transformation and intensive vector algebra. In contrast, we decompose the electromagnetic fields due to the circular loops into the corresponding vector spherical wave functions. Then, we apply the vector addition theorem [10, 11] to translate the wave functions from the secondary loop to the coordinate of the primary loop, and vice versa to derive a set of equations that satisfy the boundary conditions of the loops. The use of the vector addition theorem allows us to yield a very compact and succinct solution to the self and mutual admittances.

Once we obtain the admittances of the two-port network, we are able to draw some new insights on wireless power transfer. We investigate the optimal frequency in wireless power transfer between two loops of similar dimensions. The TE_{10} modes achieve higher power transfer efficiency. Smaller loops favor higher operating frequency while larger loops favor lower operating frequency. In addition, thinner wires favor higher operating frequency but its impact is less significant than loop dimension.

In practice, the dimension of the two loops can be asymmetric in size. In the symmetric case, the dominating modes of the loops and their coupling coincide, and TE_{10} modes achieve better efficiency. In the asymmetric case, these dominating modes can differ. For example, the transmit loop can be dominated by the 1st order harmonics while the receive loop is dominated by the 0th order harmonics, but the coupling is dominated by the 1st order harmonics. We will illustrate that higher order modes sometimes outperform the TE_{10} modes. They can be further exploited to attain higher efficiency in the future.

2. ANALYTICAL FRAMEWORK

With reference to Figure 1, we consider a transmit structure driven by a source that induces current density $\mathbf{J}_1$ on the transmit structure and $\mathbf{J}_2$ on the receive structure. The coupling between this pair of structures is modeled by a two-port network, $\bar{\mathbf{Z}}$:

$$V_1 = Z_{11}I_1 + Z_{12}I_2 \tag{1a}$$
$$V_2 = -Z_L I_2 = Z_{21}I_1 + Z_{22}I_2. \tag{1b}$$

Maximizing energy transfer between them is equivalent to finding Z_G and Z_L that maximizes the power delivered to the load Z_L while minimizing the input power into the two port. It is achieved when Z_G and Z_L are conjugate matched to the input impedance Z_{in} and the output impedance Z_{out} respectively. This condition is known as the *simultaneous conjugate matching*.

Solving the following simultaneous equations:

$$Z_G^* = Z_{11} - \frac{Z_{12}Z_{21}}{Z_{22} + Z_L} \quad Z_L^* = Z_{22} - \frac{Z_{12}Z_{21}}{Z_{11} + Z_G},$$

yields the optimal impedances

$$Z_{G,opt} = R_1 K + iX_1\left(1 - \frac{\text{Im } Z_{12}^2}{2R_2 X_1}\right) \quad Z_{L,opt} = R_2 K + iX_2\left(1 - \frac{\text{Im } Z_{12}^2}{2R_1 X_2}\right) \tag{2}$$

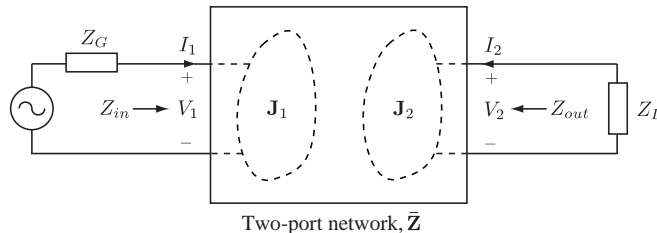Two-port network, $\bar{\mathbf{Z}}$

Figure 1. Models the coupling between the transmit and receive structures as a two-port network, $\bar{\mathbf{Z}}$.

where $Z_{nn} = R_n - iX_n$ and

$$K = \sqrt{1 - \frac{\text{Re } Z_{12}^2}{R_1 R_2} - \left(\frac{\text{Im } Z_{12}^2}{2R_1 R_2}\right)^2}.$$

The optimal efficiency is therefore given by

$$\eta_{opt} = \frac{|Z_{12}|^2}{2(1+K)R_1 R_2 - \text{Re } Z_{12}^2}. \tag{3}$$

In this paper, we will use η_{opt} as a figure of merit in the performance analyses. Various forms of RLC networks in RF circuit design [12] can be implemented to synthesize $Z_{G,opt}$ and $Z_{L,opt}$.

3. SELF AND MUTUAL ADMITTANCES OF TWO CIRCULAR LOOPS

In this section, we will first define self and mutual admittances in terms of the harmonics of the loops. Then, we solve the admittances by satisfying a set of boundary conditions based on the technique of method of moments.

3.1. Definition of Self and Mutual Admittances

We rewrite (1) in terms of the self and mutual admittances:

$$I_1 = Y_{11}V_1 + Y_{12}V_2 \tag{4a}$$
$$I_2 = Y_{21}V_1 + Y_{22}V_2. \tag{4b}$$

The self admittance Y_{11} is obtained when a voltage source V_1 is applied to loop 1 and loop 2 is shorted ($V_2 = 0$), as illustrated in Figure 2(a). Suppose that the loop is thin. The induced current density on loop 1 can be modeled as

$$\mathbf{J}_{11}(\mathbf{r}) = \hat{\boldsymbol{\phi}} J_{11,\phi}(\phi) \frac{\delta(\theta - \pi/2)}{r} \delta(r - l). \tag{5}$$

The ϕ dependence can be expanded by the orthogonal basis $\{e^{im\phi}\}$:

$$J_{11,\phi}(\phi) = \sum_{m=-\infty}^{\infty} x_{m,11} e^{im\phi}. \tag{6}$$

The self admittance Y_{11} is then given by

$$Y_{11} = \frac{J_{11,\phi}(0)}{V_1} = \frac{\sum\limits_{m=-\infty}^{\infty} x_{m,11}}{V_1}. \tag{7}$$

Suppose that loop 1 is centered at the origin and loop 2 is at $\mathbf{r}_{12}$. The current induced on loop 2 satisfies

$$\mathbf{J}_{21}(\mathbf{r} - \mathbf{r}_{12}) = \hat{\boldsymbol{\phi}} J_{21,\phi}(\phi) \frac{\delta(\theta - \pi/2)}{r} \delta(r - l) \tag{8}$$
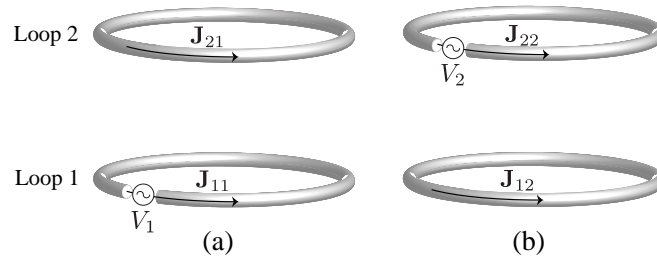

Figure 2. (a) To define Y_{11} and Y_{12}, a voltage source is applied to loop 1 and loop 2 is shorted; and (b) to define Y_{22} and Y_{21}, a voltage source is applied to loop 2 and loop 1 is shorted.

and

$$J_{21,\phi}(\phi) = \sum_{m=-\infty}^{\infty} x_{m,21} e^{im\phi}. \tag{9}$$

The mutual admittance Y_{21} is then given by

$$Y_{21} = \frac{\displaystyle\sum_{m=-\infty}^{\infty} x_{m,21}}{V_1}. \tag{10}$$

Similarly, we can obtain Y_{12} and Y_{22} by applying a voltage source V_2 to loop 2 while shorting loop 1, as illustrated in Figure 2(b).

3.2. Analytical Solutions based on Method of Moments (MOM)

The set of Fourier coefficients $\{x_{\mu,nm}\}$ for μ, n, $m = 1$, 2 are determined by satisfying the boundary conditions. Suppose that the loops are made of material with finite conductivity σ, and l_n, a_n, and $A_{w,n}$ are the loop radius, wire radius, and effective cross sectional area[†], respectively. We assume that $a_n \ll l_n$ and a_n is much less than a wavelength such that we can use the delta-gap model to model the feed region. Let us first consider the scenario in Figure 2(a) and denote the electric field from $\mathbf{J}_{nm}$ by $\mathbf{E}_{nm}$ for n, $m = 1$, 2. The ϕ direction of the electric field is required to satisfy:

$$E_{11,\phi}(l_1 + a_1, \pi/2, \phi) + E_{21,\phi}(l_1 + a_1, \pi/2, \phi) = \frac{J_{11,\phi}(\phi)}{\sigma A_{w,1}} - \frac{V_1 \delta(\phi)}{l_1 + a_1} \tag{11}$$

and

$$E_{11,\phi}(\mathbf{r}) + E_{21,\phi}(\mathbf{r}) = \frac{J_{21,\phi}(\phi)}{\sigma A_{w,2}}, \quad \forall \mathbf{r} \in \{\mathbf{r} : \mathbf{r} - \mathbf{r}_{12} = (l_2 + a_2, \pi/2, \phi) \text{ for some } \phi\}. \tag{12}$$

To derive the electric fields, let us first introduce the vector spherical wave functions, $\mathbf{M}_{nm}(\mathbf{r})$ and $\mathbf{N}_{nm}(\mathbf{r})$. From definitions and results from [13],

$$\mathbf{M}_{nm}(\mathbf{r}) = h_n^{(1)}(kr) r \nabla Y_{nm}(\theta, \phi) \times \hat{\mathbf{r}} \tag{13a}$$

$$\mathbf{N}_{nm}(\mathbf{r}) = n(n+1) \frac{h_n^{(1)}(kr)}{kr} Y_{nm}(\theta, \phi) \hat{\mathbf{r}} + \left[h_{n-1}^{(1)}(kr) - n \frac{h_n^{(1)}(kr)}{kr} \right] r \nabla Y_{nm}(\theta, \phi). \tag{13b}$$

Furthermore, we introduce the operator R_g. When it acts on $\mathbf{M}_{nm}(\mathbf{r})$ and $\mathbf{N}_{nm}(\mathbf{r})$, the spherical Hankel function $h_n^{(1)}(\cdot)$ is replaced by the spherical Bessel function $j_n(\cdot)$. Denote the projection of the ϕ component of $R_g \mathbf{M}_{nm}(\mathbf{r})$ and $R_g \mathbf{N}_{nm}(\mathbf{r})$ onto the basis of the source current $e^{-im\phi}$ by

$$p_{1nm}(l) = kl \int R_g M_{nm,\phi}(l, \pi/2, \phi) e^{-im\phi} d\phi \tag{14a}$$

$$p_{2nm}(l) = kl \int R_g N_{nm,\phi}(l, \pi/2, \phi) e^{-im\phi} d\phi. \tag{14b}$$

Note that $p_{\kappa,n,-m}(l) = (-1)^m p_{\kappa nm}^*(l)$. The electric fields are given by

$$\mathbf{E}_{11}(\mathbf{r}) = -k\eta \sum_{n=1}^{\infty} \sum_{m=-n}^{n} \frac{x_{m,11}}{n(n+1)} \left[p_{1nm}^*(l_1) \mathbf{M}_{nm}(\mathbf{r}) + p_{2nm}^*(l_1) \mathbf{N}_{nm}(\mathbf{r}) \right] \tag{15a}$$

$$\mathbf{E}_{21}(\mathbf{r}) = -k\eta \sum_{n=1}^{\infty} \sum_{m=-n}^{n} \frac{x_{m,21}}{n(n+1)} \left[p_{1nm}^*(l_2) \mathbf{M}_{nm}(\mathbf{r} - \mathbf{r}_{12}) + p_{2nm}^*(l_2) \mathbf{N}_{nm}(\mathbf{r} - \mathbf{r}_{12}) \right]. \tag{15b}$$

The expression for $\mathbf{E}_{11}(\mathbf{r})$ is valid for $r > l_1$ while the expression for $\mathbf{E}_{21}(\mathbf{r})$ is valid for $r > l_2$. As $\mathbf{M}_{nm}(\mathbf{r})$ is transverse to $\mathbf{r}$, it is referred to as the TE$_{nm}$ mode. The $\mathbf{N}_{nm}(\mathbf{r})$ is referred to as the TM$_{nm}$ mode.

[†] The effective cross sectional area equals to wire perimeter times its skin depth.

The vector spherical functions $\mathbf{M}_{nm}(\mathbf{r})$ and $\mathbf{N}_{nm}(\mathbf{r})$ are orthogonal while their translated versions $\mathbf{M}_{nm}(\mathbf{r} - \mathbf{r}_{12})$ and $\mathbf{N}_{nm}(\mathbf{r} - \mathbf{r}_{12})$ are not. Applying the vector addition theorem [10, 11],

$$\mathbf{M}_{nm}(\mathbf{r} - \mathbf{r}_{12}) = n(n+1) \sum_{n',m'} \left[\alpha_{nm,n'm'}(\mathbf{r}_{12}) R_g \mathbf{M}_{n'm'}(\mathbf{r}) + \beta_{nm,n'm'}(\mathbf{r}_{12}) R_g \mathbf{N}_{n'm'}(\mathbf{r}) \right] \quad (16a)$$

$$\mathbf{N}_{nm}(\mathbf{r} - \mathbf{r}_{12}) = n(n+1) \sum_{n',m'} \left[\alpha_{nm,n'm'}(\mathbf{r}_{12}) R_g \mathbf{N}_{n'm'}(\mathbf{r}) + \beta_{nm,n'm'}(\mathbf{r}_{12}) R_g \mathbf{M}_{n'm'}(\mathbf{r}) \right] \quad (16b)$$

for $r < r_{12}$, where the coupling coefficients are given by

$$\alpha_{nm,n'm'}(\mathbf{r}_{12}) = \frac{i^{n'-n}}{n(n+1)n'(n'+1)} \sum_{n''} \left[n(n+1) + n'(n'+1) - n''(n''+1) \right] \gamma_{nm,n'm',n''}(\mathbf{r}_{12})$$

$$\beta_{nm,n'm'}(\mathbf{r}_{12}) = \frac{i^{n'-n+1}}{n(n+1)n'(n'+1)} \sum_{n''} \Big\{ kr_{12} \cos(\pi - \theta_{12}) \cdot 2m' \gamma_{nm,n'm',n''}(\mathbf{r}_{12})$$

$$+ kr_{12} \sin(\pi - \theta_{12}) \big[e^{i(\pi+\phi_{12})} \sqrt{(n'-m')(n'+m'+1)} \gamma_{nm,n'(m'+1),n''}(\mathbf{r}_{12})$$

$$+ e^{-i(\pi+\phi_{12})} \sqrt{(n'+m')(n'-m'+1)} \gamma_{nm,n'(m'-1),n''}(\mathbf{r}_{12}) \big] \Big\}$$

$$\gamma_{nm,n'm',n''}(\mathbf{r}_{12}) = (-1)^m i^{n''} Y_{n'',m-m'}(\pi - \theta_{12}, \pi + \phi_{12}) h_{n''}^{(1)}(kr_{12}) \sqrt{\pi(2n+1)(2n'+1)(2n''+1)}$$

$$\begin{pmatrix} n & n' & n'' \\ 0 & 0 & 0 \end{pmatrix} \begin{pmatrix} n & n' & n'' \\ -m & m' & m-m' \end{pmatrix}.$$

The summations over n'' increments by a step of 2 and over the range $|n - n'| \le n'' \le n + n'$. In the expression, $\begin{pmatrix} j_1 & j_2 & j_3 \\ m_1 & m_2 & m_3 \end{pmatrix}$ is the Wigner 3-j symbol, and captures the strength of the coupling among the multipoles with indices (j_1, m_1), (j_2, m_2), and (j_3, m_3). Now, $\mathbf{E}_{21}(\mathbf{r})$ can be expressed as a sum of vector spherical functions $R_g \mathbf{M}_{nm}(\mathbf{r})$ and $R_g \mathbf{N}_{nm}(\mathbf{r})$ which are orthogonal.

Denote the projection of the ϕ component of $\mathbf{M}_{nm}(\mathbf{r})$ and $\mathbf{N}_{nm}(\mathbf{r})$ onto the basis $e^{-im\phi}$ by

$$q_{1nm}(l) = kl \int M_{nm,\phi}(l, \pi/2, \phi) e^{-im\phi} d\phi \quad (17a)$$

$$q_{2nm}(l) = kl \int N_{nm,\phi}(l, \pi/2, \phi) e^{-im\phi} d\phi. \quad (17b)$$

The boundary condition (11) can be written as a set of linear algebraic equations:

$$z_{m,11} x_{m,11} + \sum_{m'=-\infty}^{\infty} z_{mm',12} x_{m',21} = V_1, \quad m = 0, \pm 1, \ldots \quad (18)$$

where

$$z_{m,11} = \frac{2\pi(l_1 + a_1)}{\sigma A_{w,1}} + \sum_{n=\max\{1,|m|\}}^{\infty} \sum_{\kappa=1}^{2} \frac{\eta}{n(n+1)} p_{\kappa nm}^*(l_1) q_{\kappa nm}(l_1 + a_1) \quad (19a)$$

$$z_{m'm,12} = \eta \sum_{n=\max\{1,|m|\}}^{\infty} \sum_{n'=\max\{1,|m'|\}}^{\infty} \Big[p_{1nm}^*(l_2) \alpha_{nm,n'm'}(\mathbf{r}_{12}) p_{1n'm'}(l_1 + a_1)$$

$$+ p_{2nm}^*(l_2) \alpha_{nm,n'm'}(\mathbf{r}_{12}) p_{2n'm'}(l_1 + a_1) + p_{1nm}^*(l_2) \beta_{nm,n'm'}(\mathbf{r}_{12}) p_{2n'm'}(l_1 + a_1)$$

$$+ p_{2nm}^*(l_2) \beta_{nm,n'm'}(\mathbf{r}_{12}) p_{1n'm'}(l_1 + a_1) \Big]. \quad (19b)$$

The first term in $z_{m'm,12}$ captures the coupling from the $\text{TE}_{n'm'}$ mode to the TE_{nm} mode; the second term captures the coupling from the $\text{TM}_{n'm'}$ mode to the TM_{nm} mode; the third term captures the coupling from the $\text{TM}_{n'm'}$ mode to the TE_{nm} mode; and the last term captures the coupling from the $\text{TE}_{n'm'}$ mode to the TM_{nm} mode.

Translating the origin of the coordinate systems to $\mathbf{r}_{12}$, the electric fields become

$$\mathbf{E}_{11}(\mathbf{r}) = -k\eta \sum_{n=1}^{\infty} \sum_{m=-n}^{n} \frac{x_{m,11}}{n(n+1)} \left[p_{1nm}^*(l_1)\mathbf{M}_{nm}(\mathbf{r}+\mathbf{r}_{12}) + p_{2nm}^*(l_1)\mathbf{N}_{nm}(\mathbf{r}+\mathbf{r}_{12}) \right] \tag{20a}$$

$$\mathbf{E}_{21}(\mathbf{r}) = -k\eta \sum_{n=1}^{\infty} \sum_{m=-n}^{n} \frac{x_{m,21}}{n(n+1)} \left[p_{1nm}^*(l_2)\mathbf{M}_{nm}(\mathbf{r}) + p_{2nm}^*(l_2)\mathbf{N}_{nm}(\mathbf{r}) \right]. \tag{20b}$$

Define

$$z_{m,22} = \frac{2\pi(l_2+a_2)}{\sigma A_{w,2}} + \sum_{n=\max\{1,|m|\}}^{\infty} \sum_{\kappa=1}^{2} \frac{\eta}{n(n+1)} p_{\kappa nm}^*(l_2) q_{\kappa nm}(l_2+a_2) \tag{21a}$$

$$z_{m'm,21} = \eta \sum_{n=\max\{1,|m|\}}^{\infty} \sum_{n'=\max\{1,|m'|\}}^{\infty} \left[\sum_{\kappa=1}^{2} p_{\kappa nm}^*(l_1)\alpha_{nm,n'm'}(-\mathbf{r}_{12})p_{\kappa n'm'}(l_2+a_2) \right.$$
$$\left. + p_{1nm}^*(l_1)\beta_{nm,n'm'}(-\mathbf{r}_{12})p_{2n'm'}(l_2+a_2) + p_{2nm}^*(l_1)\beta_{nm,n'm'}(-\mathbf{r}_{12})p_{1n'm'}(l_2+a_2) \right]. \tag{21b}$$

The boundary condition (12) can be written concisely as

$$\sum_{m'=-\infty}^{\infty} z_{mm',21}x_{m',11} + z_{m,22}x_{m,21} = 0, \quad m = 0, \pm 1, \ldots. \tag{22}$$

Furthermore, the boundary conditions (18) and (22) can be written more concisely in matrix form as

$$\bar{\mathbf{Z}}_{11}\mathbf{x}_{11} + \bar{\mathbf{Z}}_{12}\mathbf{x}_{21} = V_1\mathbf{1} \tag{23a}$$

$$\bar{\mathbf{Z}}_{21}\mathbf{x}_{11} + \bar{\mathbf{Z}}_{22}\mathbf{x}_{21} = \mathbf{0} \tag{23b}$$

where $\mathbf{1}$ is a vector of all ones,

$$\bar{\mathbf{Z}}_{\nu\nu} = \begin{bmatrix} \ddots & \vdots & \vdots & \vdots & \\ \cdots & z_{-1,\nu\nu} & 0 & 0 & \cdots \\ \cdots & 0 & z_{0,\nu\nu} & 0 & \cdots \\ \cdots & 0 & 0 & z_{1,\nu\nu} & \cdots \\ & \vdots & \vdots & \vdots & \ddots \end{bmatrix} \quad \bar{\mathbf{Z}}_{\nu\mu} = \begin{bmatrix} \ddots & \vdots & \vdots & \vdots & \\ \cdots & z_{-1,-1,\nu\mu} & z_{-1,0,\nu\mu} & z_{-1,1,\nu\mu} & \cdots \\ \cdots & z_{0,-1,\nu\mu} & z_{00,\nu\mu} & z_{01,\nu\mu} & \cdots \\ \cdots & z_{1,-1,\nu\mu} & z_{10,\nu\mu} & z_{11,\nu\mu} & \cdots \\ & \vdots & \vdots & \vdots & \ddots \end{bmatrix} \tag{24}$$

and

$$\mathbf{x}_{\nu\mu} = [\cdots \quad x_{-1,\nu\mu} \quad x_{0,\nu\mu} \quad x_{1,\nu\mu} \quad \cdots]^t.$$

This yields

$$\mathbf{x}_{11} = V_1 \left(\bar{\mathbf{Z}}_{11} - \bar{\mathbf{Z}}_{12}\bar{\mathbf{Z}}_{22}^{-1}\bar{\mathbf{Z}}_{21} \right)^{-1} \mathbf{1} \tag{25a}$$

$$\mathbf{x}_{21} = V_1 \left(\bar{\mathbf{Z}}_{12} - \bar{\mathbf{Z}}_{11}\bar{\mathbf{Z}}_{21}^{-1}\bar{\mathbf{Z}}_{22} \right)^{-1} \mathbf{1}. \tag{25b}$$

Hence,

$$Y_{11} = \mathbf{1}^t \left(\bar{\mathbf{Z}}_{11} - \bar{\mathbf{Z}}_{12}\bar{\mathbf{Z}}_{22}^{-1}\bar{\mathbf{Z}}_{21} \right)^{-1} \mathbf{1} \tag{26a}$$

$$Y_{21} = \mathbf{1}^t \left(\bar{\mathbf{Z}}_{12} - \bar{\mathbf{Z}}_{11}\bar{\mathbf{Z}}_{21}^{-1}\bar{\mathbf{Z}}_{22} \right)^{-1} \mathbf{1}. \tag{26b}$$

Similarly, when we apply the above derivation to the scenario in Figure 2(b), we obtain

$$Y_{22} = \mathbf{1}^t \left(\bar{\mathbf{Z}}_{22} - \bar{\mathbf{Z}}_{21}\bar{\mathbf{Z}}_{11}^{-1}\bar{\mathbf{Z}}_{12} \right)^{-1} \mathbf{1} \tag{27a}$$

$$Y_{12} = \mathbf{1}^t \left(\bar{\mathbf{Z}}_{21} - \bar{\mathbf{Z}}_{22}\bar{\mathbf{Z}}_{12}^{-1}\bar{\mathbf{Z}}_{11} \right)^{-1} \mathbf{1}. \tag{27b}$$

3.3. Coaxial Loops

When the loops are coaxial, $\alpha_{nm,n'm'}$ and $\beta_{nm,n'm'}$ are non-zero only if $m = m'$. The matrices $\bar{\mathbf{Z}}_{12}$ and $\bar{\mathbf{Z}}_{21}$ are diagonal. The admittances simplify to

$$Y_{11} = \sum_{m=-\infty}^{\infty} \frac{z_{m,22}}{z_{m,11}z_{m,22} - z_{mm,12}z_{mm,21}} \tag{28a}$$

$$Y_{21} = -\sum_{m=-\infty}^{\infty} \frac{z_{mm,21}}{z_{m,11}z_{m,22} - z_{mm,12}z_{mm,21}} \tag{28b}$$

$$Y_{12} = -\sum_{m=-\infty}^{\infty} \frac{z_{mm,12}}{z_{m,11}z_{m,22} - z_{mm,12}z_{mm,21}} \tag{28c}$$

$$Y_{22} = \sum_{m=-\infty}^{\infty} \frac{z_{m,11}}{z_{m,11}z_{m,22} - z_{mm,12}z_{mm,21}}. \tag{28d}$$

Let us define the impedance matrix for the mth harmonics by

$$\bar{\mathbf{Z}}_m = \begin{bmatrix} z_{m,11} & z_{mm,12} \\ z_{mm,21} & z_{m,22} \end{bmatrix}. \tag{29}$$

Each term inside the summation of (28) corresponds to the admittance of the mth harmonics. As a result, the resultant two-port network $\bar{\mathbf{Z}}$ is a combined network of $\bar{\mathbf{Z}}_m$'s connected in parallel. For ease of exposition, all numerical examples presented later are computed assuming coaxial loops.

3.4. General Solutions

In deriving (27), we assume that the feed region of loop 2 aligns with that of loop 1. If the feed region of loop 2 is not at $\phi = 0$ but at $\phi = \phi_2$, then V_2 in the derivation should be replaced by $V_2 e^{im\phi_2}$ and $V_2\mathbf{1}$ becomes

$$V_2 \begin{bmatrix} \ldots e^{-im\phi_2} & \ldots & 1 & \ldots & e^{im\phi_2} & \ldots \end{bmatrix}^t.$$

Furthermore in (16), we consider only the translation operator, that is, the axes of the two loops are in parallel. For arbitrary direction of the axis of loop 2 with respect to that of loop 1, we can first apply the rotation operator to the vector spherical wave functions to align the axis of loop 2 to be in parallel with that of loop 1. Then, we apply the translation operator in (16), and followed by either another rotation operator to align the feed region of both loops or changing V_2 accordingly. Finally, the derivations of the self and mutual admittances assume $r_{12} > l_1, l_2$. For all other cases, we have to interchange the spherical Bessel and Hankel functions in the definitions of $z_{m,\nu\nu}$, $z_{mm',\nu\mu}$ and $\gamma_{nm,n'm',n''}(\cdot)$ according to [14, Appendix D].

In summary, our proposed approach in solving the self and mutual admittances is very general, and applies to arbitrary loop radii, transmission range, alignment between the loops, and dielectric properties of a homogeneous isotropic medium.

4. OPTIMAL FREQUENCY FOR SYMMETRIC COILS

Here, we compute η_{opt} between symmetric loops of various loop radii and wire radii. Figure 3(a) plots the power transfer efficiency versus frequency for loop radius of $10\,\text{cm}$ and transmit-receive separation of $80\,\text{cm}$. The ratio of wire radius to loop radius varies from 0.1 to 0.01. Similarly, Figure 3(b) plots the same set of curves for loop radius of $1\,\text{cm}$ and transmit-receive separation of $8\,\text{cm}$. The power transfer efficiency first increases with frequency. After reaching an optimal frequency, it decreases with frequency more abruptly. In summary, smaller loops favor higher operating frequency while larger loops favor lower operating frequency.

Before reaching the optimal frequency, wire radius has significant impact on the efficiency. Thicker wire yields higher efficiency. After the optimal frequency, the set of curves converge as radiation loss
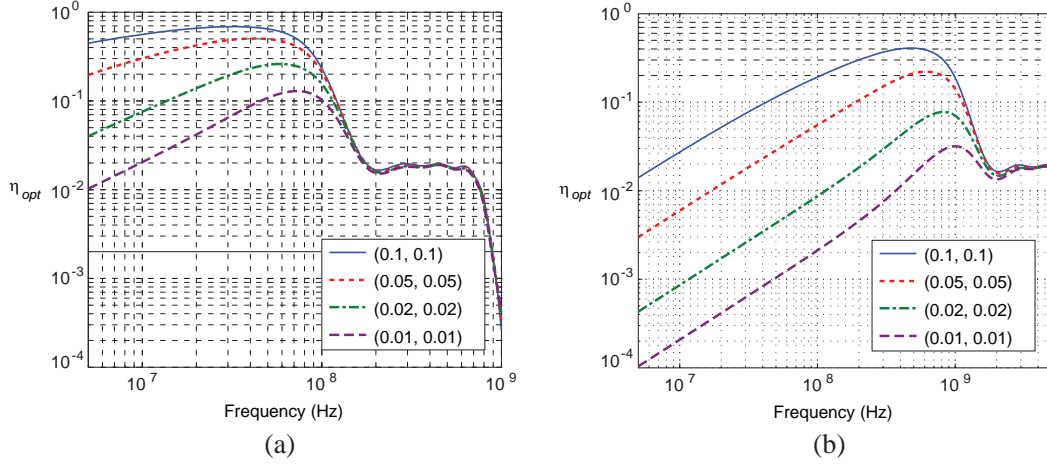
Figure 3. Plots η_{opt} versus frequency for (a) $l_1 = l_2 = 10$ cm and $r_{12} = 80$ cm, and (b) $l_1 = l_2 = 1$ cm and $r_{12} = 8$ cm. Each curve in the graph corresponds to different $(\frac{a_1}{l_1}, \frac{a_2}{l_2})$.

dominates. Let us look into the efficiency before the optimal frequency, and draw the equivalence between thicker wire and multi-turn coils. For a loop radius of 10 cm, if $\frac{a}{l} = 0.1$, the wire radius will be 1 cm. In practice, it can be too thick. Now, we can use a thinner wire but increase the number of turns. Suppose that N is the number of turns on both coils. The mutual impedance $|Z_{12}|$ increases with N^2 while the self resistances R_1, R_2 increases with N. Hence, $\frac{|Z_{21}|^2}{R_1 R_2}$ increase with N^2. This holds as long as the total length of the wire Nkl satisfies the condition for the small-antenna approximation. When the loop radii remain the same, the operating frequency needs to be reduced by N times. As $\frac{|Z_{21}|^2}{R_1 R_2} \propto f$, the net result is that $\frac{|Z_{21}|^2}{R_1 R_2}$ only increases by a factor of N instead of N^2. Similar increase can be achieved by the use of single-turn loops with wire radii increased by $\sqrt{N}$. The corresponding cross-sectional area is the same as the total cross-sectional area of the multi-turn coil.

5. HIGH-ORDER MODES

Near-field coupling focuses on power transmission between 0th order harmonics. Since the general solution derived in Section 3 includes higher order harmonics, we will investigate their impact on wireless power transfer.

5.1. Case 1: $l_1 \sim l_2$

First, we will reexamine the scenarios in Figure 3 — the loops are of similar dimensions while the transmission range is several times larger. Let us begin with reviewing the impedance matrix of the 0th order harmonics $\bar{\mathbf{Z}}_0$ defined in (29). Its elements are defined in (19) and (21). From which, if we only consider $n, n' = 1$, the resultant impedance matrix captures the coupling between the TE_{10} mode of the transmit and the receive loops. The corresponding efficiency is plotted in Figure 4 (the long-dashed curve) for $l_1 = l_2 = 10$ cm, $r_{12} = 80$ cm, and $\frac{a_1}{l_1} = \frac{a_2}{l_2} = 0.1$. In the graph, we also reproduce the curve from Figure 3(a) (the solid curve). It is the efficiency when all modes are taken into account, and is tracked closely by the efficiency of the TE_{10} mode until around 200 MHz.

After 200 MHz, the 1st order harmonics become increasingly significant. Therefore, the efficiency does not follow the trajectory of the TE_{10} mode. In the calculation of the impedances, if we sum over $n, n' \leq 2$ and $m \leq 1$, the resultant impedance matrix captures the contribution from TE_{10}, TM_{11}, and TE_{21} modes. The corresponding efficiency is plotted in Figure 4 as the dash-dotted curve. It tracks the efficiency curve closely until around 700 MHz. The 2nd order harmonics become increasingly significant. The contribution from TE_{nm} and TM_{nm} modes for $n \leq 3, m \leq 2$ is plotted in Figure 4 as the short-dashed curve. It tracks the abrupt decrease of the efficiency after 700 MHz.
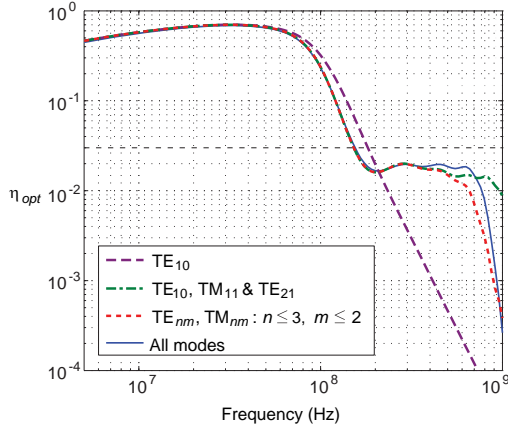
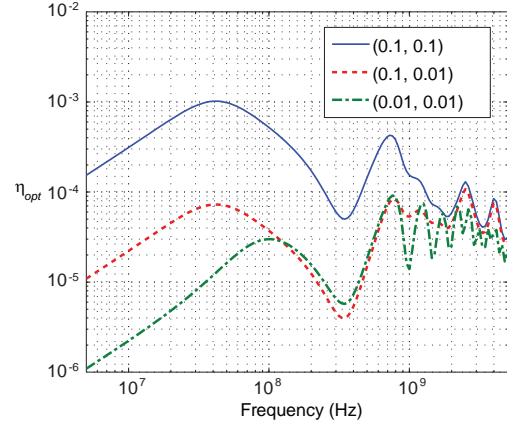**Figure 4.** Investigates the dominating modes at various frequencies.

Figure 5. Plots η_{opt} versus frequency for $l_1 = 10\,\text{cm}$, $l_2 = 1\,\text{cm}$, and $r_{12} = 80\,\text{cm}$. Each curve in the graph corresponds to different $(\frac{a_1}{l_1}, \frac{a_2}{l_2})$.

In addition, we also observe that when the 1st order harmonics become significant, both TM_{11}, and TE_{21} modes contribute more or less equally. That is, both magnetic field and electric field in the vicinity of the receive loop take part in the power transfer. Similarly, when the 2nd order harmonics become significant, the TM_{22}, TE_{30}, TM_{31}, and TE_{32} modes contribute approximately equally. On the contrary, when the 0th order harmonics are significant, magnetic field dominates.

5.2. Case 2: $l_1 \gg l_2$

When the transmit and receive loops are of comparable dimension, the dominating modes of the transmit loop coincide with those of the receive loop. These modes also dominate the coupling between the two loops. Exciting the TE_{10} modes achieves higher power transfer efficiency, in general. However, when the transmit loop is much larger than the receive loop, their dominating modes can differ and they might not be the modes dominating the coupling between the two loops. We are interested in investigating if exciting higher order modes achieves better efficiency.

Figure 5 plots the power transfer efficiency versus frequency for transmit loop radius of $10\,\text{cm}$, receive loop radius of $1\,\text{cm}$, and transmit-receive separation of $80\,\text{cm}$ with different wire radii. The set of curves roughly converge at around $2\,\text{GHz}$. In Figure 3(b), when both transmit and receive loop radii are $1\,\text{cm}$, the set of curves also converge at around $2\,\text{GHz}$. When $(\frac{a_1}{l_1}, \frac{a_2}{l_2}) = (0.1, 0.01)$, efficiencies of higher order modes are comparable with that of TE_{10} mode. They outperform the TE_{10} mode when $(\frac{a_1}{l_1}, \frac{a_2}{l_2}) = (0.01, 0.01)$. Hence, thinner loops favor higher order modes.

Recall that $x_{m,11}$ and $x_{m,22}$ capture the contribution of the mth harmonics on the self impedance of the transmit and the receive loops respectively. As the loops are coaxial, the coupling between the mth transmit and the m'th receive harmonics are nonzero only if $m = m'$. The $x_{m,12}$ captures the strength of the coupling between the mth transmit and mth receive harmonics. Figure 6 plots the magnitude of $x_{m,11}$, $x_{m,22}$, and $x_{m,12}$ versus frequency. Below $300\,\text{MHz}$, the transmit loop, the receive loop, and the coupling are dominated by the 0th order harmonics. In between $300\,\text{MHz}$ and $800\,\text{MHz}$, the transmit loop is dominated by the 1st order harmonics while the receive loop is dominated by the 0th order harmonics. The coupling is dominated by the 1st order harmonics. Hence, the admittances can be approximated by

$$Y_{11} \approx \frac{x_{-1,11} + x_{1,11}}{V_1} \quad Y_{12} = Y_{21} \approx \frac{x_{-1,21} + x_{1,21}}{V_1} \quad Y_{22} \approx \frac{x_{0,22}}{V_2}. \tag{30}$$

From (25), we have

$$x_{-1,11} = x_{1,11} \approx \frac{V_1}{z_{1,11}} \quad x_{-1,21} = x_{1,21} \approx -\frac{z_{11,21} V_1}{z_{1,11} z_{1,22}} \quad x_{0,22} \approx \frac{V_2}{z_{0,22}}. \tag{31}$$
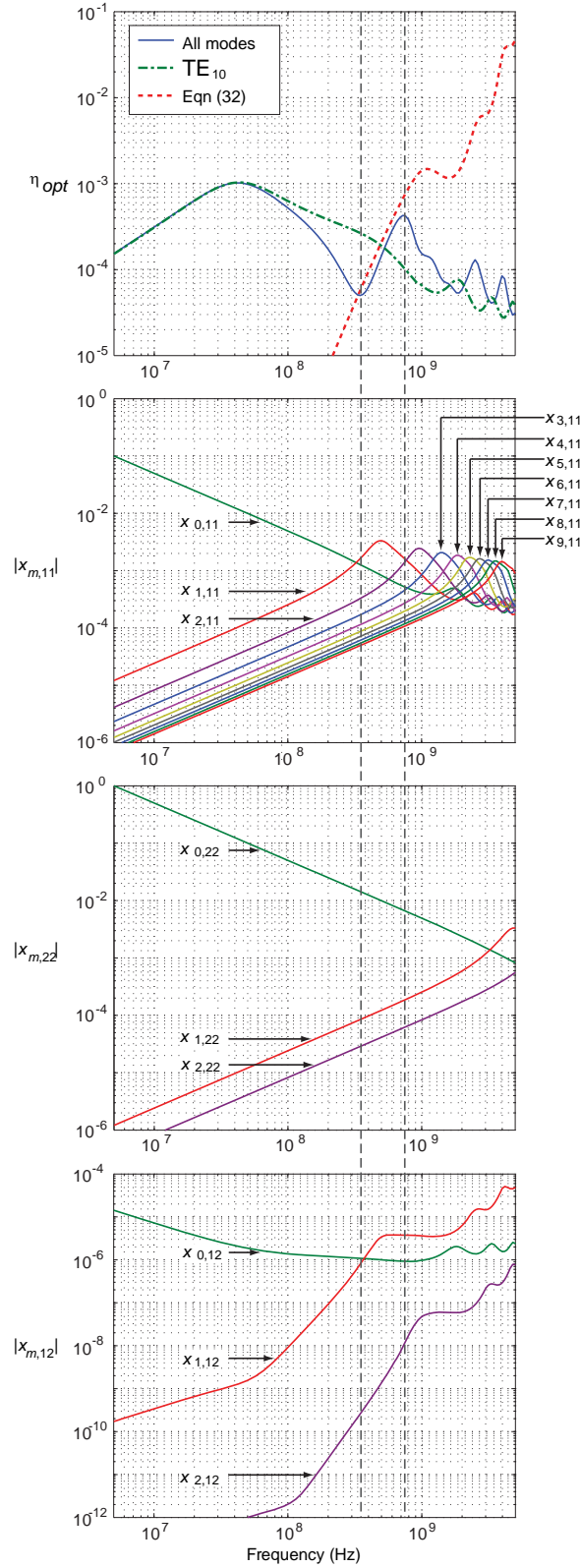
Figure 6. The top figure plots the approximated efficiency in (32) versus frequency and the exact efficiency curve. It also includes the efficiency curve of TE_{10} modes. The bottom three figures plot the magnitude of $x_{m,11}$, $x_{m,22}$, and $x_{m,12}$ versus frequency. In between the two dashed vertical lines defines the range of frequency where the transmit loop is dominated by the 1st order harmonics.

Consequently, the optimal efficiency can be approximated by

$$\eta_{opt} \approx \frac{|Y_{12}|^2}{4\,\mathrm{Re}\,Y_{11}\,\mathrm{Re}\,Y_{22}} \approx \frac{|2z_{11,21}|^2}{4\,\mathrm{Re}(2z_{1,11})\,\mathrm{Re}\,z_{0,22}}\left|\frac{x_{1,22}}{x_{0,22}}\right|^2. \tag{32}$$

In Figure 6, we plot this approximated efficiency for $(\frac{a_1}{l_1}, \frac{a_2}{l_2}) = (0.1, 0.1)$ (the dashed curve). It tracks the efficiency curve closely in between 300 MHz and 800 MHz.

The first factor in (32) is the approximated efficiency of a two-port network with self impedances $2z_{1,11}, z_{0,22}$ and mutual impedance $2z_{11,21}$. It is then weighted by the second factor which is the ratio of $|x_{1,22}|^2$ to $|x_{0,22}|^2$. In general, when the dominating mode of the receive loop is the 0th order harmonics, the optimal efficiency can be approximated by

$$\eta_{opt} \approx \frac{|2z_{11,21}|^2}{4\,\mathrm{Re}(2z_{m,11})\,\mathrm{Re}\,z_{0,22}}\left|\frac{x_{1,22}}{x_{0,22}}\right|^2\left|\frac{x_{1,11}}{x_{m,11}}\right|^2 \tag{33}$$

where m is the dominating harmonic of the transmit loop at the frequency range of interest. As $|x_{1,22}| \ll |x_{0,22}|$ and $|x_{1,11}| \ll |x_{m,11}|$, if we are able to redistribute the mode contributions on the transmit and the receive loops, higher efficiency can be attained. For example, in between 800 MHz and 3 GHz, if we can excite the 1st order harmonics on the transmit loop while suppress the other modes, the efficiency will approach (32) and will potentially outperform that of TE_{10} modes.

6. CONCLUSIONS

Wireless technologies have transformed the telecommunication industry. Wireless power transfer is expected to bring wireless technologies to a new era of truly wireless in mobile devices. In the past, long-haul power transmission schemes were researched. Recently, interests have shifted to contactless power charger for mobile devices and short-distance power transmission schemes. This paper provides an analytical framework that spans both spectrum of applications. Via the general solution, we conclude that when the transmit and receive loops are of similar dimension, TE_{10} mode and near-field approximations suffice to obtain the optimal solution. When there is asymmetry in the loop dimensions, higher order modes might outperform TE_{10} modes. The efficiency can be further improved if we are able to manipulate the mode distributions on the larger loop.

REFERENCES

1. Tesla, N., "Experiments with alternate currents of very high frequency and their application to methods of artificial illumination," Lecture, American Institute of Electrical Engineers, Columbia College, NY, May 20, 1891.
2. "Apparatus for transmission of electrical energy," US Patent US 649–621, May 15, 1900.
3. Kurs, A., A. Karalis, R. Moffatt, J. D. Joannopoulos, P. Fisher, and M. Soljacic, "Wireless power transfer via strongly coupled magnetic resonances," *Science*, Vol. 317, 83–86, Jul. 2007.
4. Karalis, A., J. D. Joannopoulos, and M. Soljacic, "Efficient wireless non-radiative mid-range energy transfer," *Ann. Phys.*, Vol. 323, No. 1, 34–48, Jan. 2008.
5. Brown, W. C., "The history of power transmission by radio waves," *IEEE Trans. Microwave Theory Tech.*, Vol. 32, No. 9, 1230–1242, Sep. 1984.
6. Brown, W. C. and E. E. Eyes, "Beamed microwave power transmission and its application to space," *IEEE Trans. Microwave Theory Tech.*, Vol. 40, No. 6, 1239–1250, Jun. 1992.
7. Iizuka, K., R. W. P. King, and J. C. W. Harrison, "Self- and mutual admittances of two identical circular loop antennas in a conducting medium and in air," *IEEE Trans. Antennas Propag.*, Vol. 14, No. 4, 440–450, Jul. 1966.
8. Ito, S., N. Inagaki, and T. Sekiguchi, "An investigation of the array of circular-loop antennas," *IEEE Trans. Antennas Propag.*, Vol. 19, No. 4, 469–476, Jul. 1971.
9. Krishnan, S., L.-W. Li, and M.-S. Leong, "Entire-domain MoM analysis of an array of arbitrary oriented circular loop antennas: A general formulation," *IEEE Trans. Antennas Propag.*, Vol. 53, No. 9, 2961–2968, Sep. 2005.

10. Danos, M. and L. C. Maximon, "Multipole matrix elements of the translation operator," *J. Math. Phys.*, Vol. 6, No. 5, 766–778, May 1965.

11. He, B. and W. C. Chew, "Addition theorem," *Modeling and Computations in Electromagnetics: Lecture Notes in Computational Science and Engineering*, Vol. 59, 203–226, 2008.

12. Lee, T. H., *The Design of CMOS Radio-frequency Integrated Circuits*, 2nd Edition, Cambridge University Press, 2003.

13. Barrera, R. G. G. A. Estévez, and J. Giraldo, "Vector spherical harmonics and their application to magnetostatics," *Eur. J. Phys.*, Vol. 6, 287–294, 1985.

14. Chew, W. C., *Waves and Fields in Inhomogeneous Media*, IEEE Press, 1995.